International Journal of Fatigue 193 (2025) 108814

Contents lists available at ScienceDirect

International Journal of Fatigue

journal homepage: www.elsevier.com/locate/ijfatigue

Ausformed high-strength low-alloy steel exhibits exceptional resistance to fatigue crack-growth in high-pressure hydrogen environments

Timothee Redarce [a,*], Keiichiro Iwata [a], Yuhei Ogawa [b], Kaneaki Tsuzaki [b], Akinobu Shibata [b], Hisao Matsunaga [c,d]

[a] Graduate School of Engineering, Kyushu University, Japan
[b] Research Center for Structural Materials, National Institute for Materials Science, Japan
[c] Department of Mechanical Engineering, Kyushu University, Japan
[d] Research Center for Hydrogen Industrial Use and Storage (HYDROGENIUS), Kyushu University, Japan

ARTICLE INFO

Keywords:
Hydrogen embrittlement
High-strength low-alloy steel
Ausforming
Fatigue crack-growth

ABSTRACT

Ausformed specimens of the chromium-molybdenum steel JIS-SCM440 were subjected to fatigue tests in both air and 90 MPa hydrogen gas. The results were compared with those of non-ausformed specimens of the same material with similar tensile strengths (≈ 950 MPa and ≈ 1050 MPa). The ausformed materials demonstrated excellent resistance to hydrogen-induced acceleration of fatigue crack-growth (FCG), effectively reducing the crack propagation rate under cyclic loading in hydrogen environments compared to their non-ausformed counterparts. They maintained an acceleration ratio (*i.e.*, relative FCG rate in hydrogen with respect to that in air) within 10 to 40 times, an order of magnitude lower than that of the non-ausformed counterparts. Despite their high strength levels (i.e., tensile strengths greater than 900 MPa), the FCG rate in the ausformed materials was almost independent of loading frequency at a stress intensity factor range of 20 and 30 MPa·m$^{1/2}$. Fractographic observations revealed that no intergranular fracture occurred in the ausformed materials, unlike in the non-ausformed ones. These findings suggest that two factors possibly caused the mitigation of FCG rate in hydrogen: (i) modification of the microstructure morphology, i.e., refinement and elongation, and (ii) an increase in the cohesive strength of interfaces under the influence of hydrogen.

1. Introduction

As the world advances towards decarbonization, hydrogen has emerged as a promising alternative to fossil fuels in various applications. However, the high cost of materials used in hydrogen production, storage, and transportation remains a significant barrier to its widespread adoption. Such expensive materials are primarily employed to counteract a phenomenon known as hydrogen embrittlement (HE), where the mechanical properties of metallic materials are significantly degraded by solute hydrogen [1–8]. This degradation can lead to unexpected and catastrophic failures in structures or components subjected to mechanical stress and strain [9,10].

The severity of HE depends on materials (e.g., material type [11], microstructure [8], strength level [12–14]) as well as environmental conditions (e.g., pressure [15], temperature [16,17], gas impurities [18–20]). As a result, preventing and mitigating HE is a complex challenge that requires a multidisciplinary approach involving materials science, corrosion science, and mechanical engineering [21]. However, understanding the influence of hydrogen on strength properties and their underlying mechanisms has enabled the development of effective strength design for high-pressure hydrogen components. Additionally, to reduce costs and improve the performance of these components, alternative materials are being actively investigated.

Higher-strength steels offer numerous advantages, such as improved safety, increased capacity, weight reduction, longer lifecycles, and enhanced environmental impact. However, it has been reported that low-alloy steels with higher-strength exhibit greater susceptibility to HE [12,13]. A significant acceleration in fatigue crack-growth (FCG) is observed in low-alloy steels with tensile strengths, σ_B, exceeding 900 MPa. Below this threshold, the hydrogen-induced acceleration in these steels shows little to no dependence on loading frequency, indicating that FCG life can be determined by the number of cycles, regardless of loading time. In contrast, above the 900 MPa threshold, the FCG acceleration becomes more pronounced as strength increases and loading

* Corresponding author at: Department of Mechanical Engineering, Kyushu University, 744 Motooka, Nishi-ku, Fukuoka, 819-0395 Japan.
E-mail address: redarce.tanneguy.timothee.831@m.kyushu-u.ac.jp (T. Redarce).

https://doi.org/10.1016/j.ijfatigue.2025.108814
Received 6 November 2024; Received in revised form 30 December 2024; Accepted 9 January 2025
Available online 10 January 2025

frequency decreases. In such cases, FCG life cannot be determined solely by the number of cycles, complicating fatigue life design. Unfortunately, commercial low-alloy steels currently cannot surpass the 900 MPa threshold in a 100 MPa-class hydrogen gas environment, limiting the range of usable materials and their applicable strength levels [22].

Ausformed and tempered (AFT) steel is recognized for its excellent strength properties under the influence of hydrogen [23]. The corresponding thermomechanical treatment involves a hot working process of austenite above M_S temperature followed by quenching. A key advantage of ausforming is the increase in the strength of finally formed martensite despite minimal decreases in its toughness and ductility [24]. Many researchers have been studying the mechanisms behind these superior strength properties. Kimura et al. [25] found that AFT samples of low-alloy steel exhibited improved delayed fracture resistance compared to quench-and-tempered samples. They attributed this improvement to a finer microstructure and increased dislocation density, which hinders hydrogen diffusion in the material, thereby mitigating HE. AFT steels exhibit a distinctive microstructure; for example, the prior-austenite grain boundaries (PAGBs) have an undulating shape and varying cementite orientations along the same grain boundary, as reported by Yusa et al. [26] and Maki et al. [27], which likely contribute positively to FCG resistance. They reported that ausforming could suppress intergranular cracking in the process of delayed fracture, leading to a change in the crack path from intergranular to transgranular. It is also worth noting that ausforming can enhance the fracture resistance of materials without changing the chemical composition, allowing the use of less costly alloys for more applications. Based on these facts, AFT steels are also expected to achieve higher-strength suitable for high-pressure hydrogen components. However, no study has yet examined the strength properties of AFT materials in high-pressure hydrogen environments.

In this study, we examined the effect of the ausforming process on the FCG resistance of low-alloy steel in high-pressure hydrogen. We prepared AFT JIS-SCM440 steel at two strength levels and evaluated their FCG properties in air and 90 MPa hydrogen gas at ambient temperature using compact tension specimens. The results were compared to those of non-ausformed materials and other similar steels. The AFT materials exhibited superior performance compared to their non-ausformed counterparts. Notably, the hydrogen-induced crack acceleration in the AFT materials was nearly independent of loading frequency in the range of 0.001 to 1 Hz, even at higher-strength levels up to approximately 1050 MPa. Consequently, we conclude that AFT steels exhibit exceptional resistance to FCG in high-pressure hydrogen. This suggests that the ausforming process holds significant potential for developing higher-strength materials suitable for high-pressure hydrogen applications, through further improvements in microstructure and chemical composition, enabling more cost-efficient and higher-performance hydrogen components and systems.

2. Materials and methods

2.1. Materials

Plates of commercial-grade low-alloy chromium molybdenum steel, JIS-SCM440, were used for FCG tests. The chemical composition of the material is shown in Table 1. Steel plates with 20 mm in thickness were austenitized at a high temperature of 1000°C for 30 min in an argon gas atmosphere, air-cooled to 750°C, then compressed to 50% of their original thickness, as shown in Fig. 1(b), followed by water-quenching. The austenitization temperature of 1000°C was selected to ensure that the austenite grain size is large enough so that any diffusional transformations does not occur during air-cooling to 750°C. The temperature of the steel plates during air-cooling to 750°C was measured by a non-contact infrared-radiation thermometer. In the ausforming treatment at 750°C, the plates were first held between two 16 mm thick tungsten-carbide plates preheated to 750°C and then compressed in a forging machine with a capacity of 3000 kN. This process allowed the steel plates to be maintained at 750°C during compression. It was decided to perform the compression of the ausforming treatment at 750°C to prevent recrystallization of the austenite and diffusional transformation during the process from compression to water quenching. The quenched steel plates were subsequently tempered at two different temperatures, 600°C and 650°C, and water-quenched. The ausformed material tempered at 600°C is referred to as AFT600, and the material tempered at 650°C is referred to as AFT650.

In addition, three non-ausformed steels were prepared from JIS-SCM440. These steels underwent the same treatment steps as the AFT materials, excluding the compression process and the austenitization temperature at 850°C, and were then tempered at three different temperatures: 550°C, 600°C and 650°C for 60 min (Fig. 1(a)). These materials are referred to as T550, T600, and T650, respectively, and collectively as QT materials.

Fig. 2 presents the nominal stress-nominal strain diagram obtained from tensile testing on tensile specimens (Fig. 3). For each material, 4 tensile specimens were prepared and tested under the same conditions, the table shows the average for each material. These test were performed on a “Shimadzu AG-X plus”. It should be noted that the nominal strain was calculated by dividing the crosshead displacement by the initial gauge length. In QT materials, decreasing the tempering temperature results in increased strength and reduced strain to failure. AFT materials exhibited similar behavior; however, a comparison between AFT650 and T650 reveals that ausforming altered the material properties, increasing σ_B by approximately 40 MPa. In contrast, the strength improvement for AFT600 compared to T600 was minimal, and its strain to failure slightly decreased.

Fig. 4 presents the microstructures of the QT and AFT materials, showing crystallographic orientation maps obtained by electron backscattered diffraction (EBSD) in a scanning electron microscope (SEM), acquired with an acceleration voltage of 15 kV and a step size of 0.15 μm. In the AFT materials (cf. Fig. 4(d) and (e)), the microstructures are more flattened compared to their QT counterparts, and some constituent structures, such as blocks, are refined. However, accurate measurement of prior-austenite grains (PAG) size and aspect ratio was not possible due to the difficulty of identifying PAG in the AFT specimens included in this study. Because of the higher austenitizing temperature of the AFT materials, initial PAG size is expected to be larger than that of the QT materials.

2.2. Experiments

Fig. 5 illustrates the shape and dimensions of the compact tension (CT) specimens used for the FCG tests. The crack plane was perpendicular to the compression plane of the ausforming process. Two types of FCG tests were conducted in accordance with the ASTM E647 [28] at ambient temperature at a stress ratio, R, of 0.1 in air and 90 MPa hydrogen gas with a purity of >99.999 %: (i) load-amplitude-constant (ΔP-constant) tests and (ii) stress intensity factor range-constant (ΔK-constant) tests. The tests in high-pressure hydrogen gas were conducted using a 100 MPa high-pressure hydrogen testing system [29]. For the tests conducted in air, a Shimadzu Servopulser EHF-EM051K1 was used.

Table 1
Chemical composition of JIS-SCM440 (mass%).

C	Si	Mn	P	S	Cu	Ni	Cr	Mo
0.41	0.20	0.61	0.014	0.003	0.010	0.06	1.02	0.17

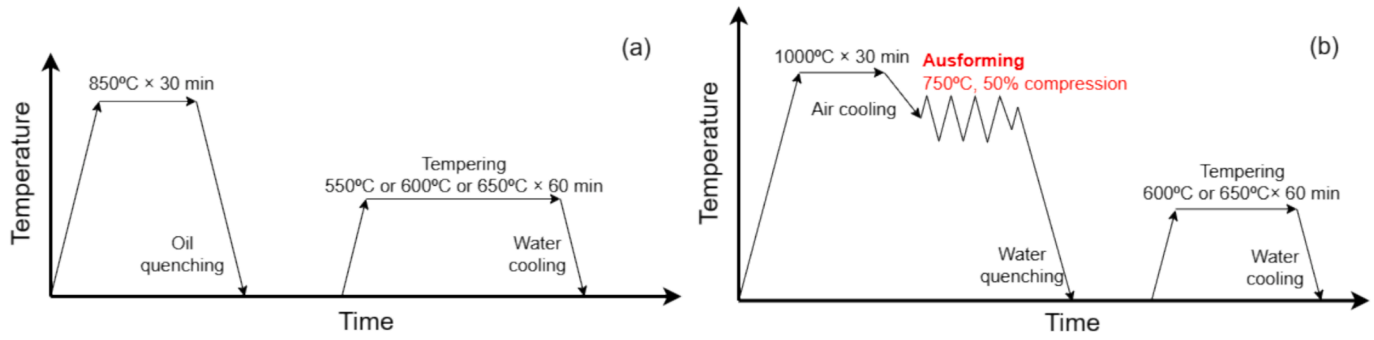

Fig. 1. Heat treatment schematics for (a) T550, T600 and T650, and (b) AFT600 and AFT650.

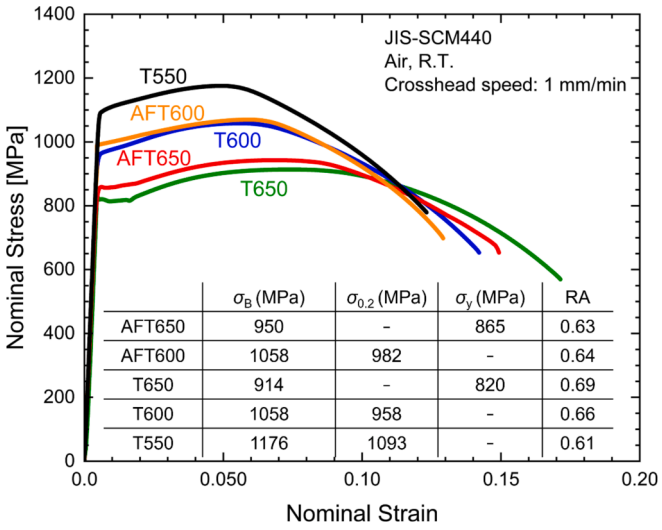

	σ_B (MPa)	$\sigma_{0.2}$ (MPa)	σ_y (MPa)	RA
AFT650	950	-	865	0.63
AFT600	1058	982	-	0.64
T650	914	-	820	0.69
T600	1058	958	-	0.66
T550	1176	1093	-	0.61

Fig. 2. Nominal stress–strain curves for QT and AFT materials.

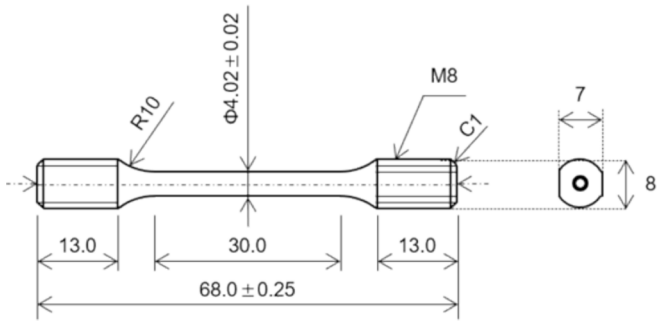

Fig. 3. Shape and dimensions of tensile specimen.

The ΔP-constant tests were performed at loading frequencies, f, of 5 Hz and 1 Hz in air and hydrogen gas, respectively. Based on the accumulated knowledge from numerous existing studies, the fatigue crack growth rate of low alloy steels in air is nearly independent of loading frequency [30–32]. Therefore, to optimize testing time, the tests in air were conducted at 5 Hz instead of 1 Hz. The ΔK and the FCG rate, da/dN, were measured using the unloading elastic compliance technique with a clip-on gauge. The ΔK-constant tests were conducted at ΔK values of 20 MPa·m$^{1/2}$ and 30 MPa·m$^{1/2}$ in 90 MPa hydrogen gas, during which the loading frequency was decreased stepwise (i.e., 1 Hz → 0.1 Hz → 0.01 Hz → 0.001 Hz). The tests in high-pressure hydrogen gas were started immediately after pressurizing the chamber with hydrogen. Following the FCG tests, the fracture surfaces were examined using a SEM with an acceleration voltage of 15 kV.

3. Results

3.1. Fatigue crack-growth behavior

Fig. 6 shows the relationship between da/dN and ΔK obtained from ΔP-constant tests in air and 90 MPa hydrogen gas. In air, the FCG rates were nearly identical for all materials, including the AFT materials. The data display linearity on a double logarithmic graph that can be depicted by the Paris-Erdogan law [33]. On the other hand, in hydrogen gas, each material exhibited a remarkable acceleration of the FCG rate, and the da/dN-ΔK curve lost its linearity. Notably, in QT materials, the FCG acceleration rate increased with an increase in the strength level. However, the acceleration in AFT materials (i.e., AFT600 and AFT650) was suppressed to lower levels than that of the QT materials. In addition, in AFT materials, the strength dependence of the hydrogen-induced FCG acceleration was less pronounced compared to QT materials. When we compare the FCG rates between AFT and QT materials, for example, the rate for AFT600 ($\sigma_B \approx 1058$ MPa) was nearly equivalent to that for T650 ($\sigma_B \approx 914$ MPa). This suggests that AFT materials have higher FCG resistance in hydrogen than QT materials when compared at an equivalent strength level.

Fig. 7 shows the relative FCG rate between air and hydrogen, $(da/dN)_H/(da/dN)_{Air}$, on a logarithmic scale as a function of loading frequency in ΔK-constant tests at $\Delta K = 20$ MPa·m$^{1/2}$, with one additional specimen of AFT600 tested at $\Delta K = 30$ MPa·m$^{1/2}$, and where $(da/dN)_H$ and $(da/dN)_{Air}$ represent the FCG rates in hydrogen and air, respectively. The relative FCG rates were calculated by comparing the FCG rate in hydrogen to that in air (cf. Fig. 6) at the same ΔK level for each material. QT materials are depicted in blue, and AFT materials are shown in red. When the relative FCG rate is plotted against loading frequency, purely cycle-dependent behavior appears as a horizontal line, indicating no dependence on loading frequency. In contrast, a purely time-dependent behavior is represented by a straight line with a negative slope, reflecting an inverse relationship between FCG rate and frequency. In the QT material T650, the acceleration rate was nearly independent of loading frequency, which is characteristic of FCG acceleration in low-to-moderate strength steels influenced by hydrogen. This behavior corresponds to the "cycle-dependent" or "time-independent" acceleration reported in literature [12,13]. It has also been reported for various carbon steels and low-alloy steels that the acceleration rate in this regime typically falls within a range of 20 to 40 times [13]. In contrast, T600 and T550 exhibit a time-dependent crack acceleration, characterized by a continuous increase in FCG as the loading frequency decreases [34]. Compared to the QT materials, all AFT materials demonstrate clear time-dependent behavior, as the acceleration rate shows only a slight increase with decreasing loading frequency (cf. Fig. 7). Even at $f = 0.001$ Hz, the acceleration rate remains around 40 times, which is within the range of the cycle-dependent acceleration in other steels. Similar to Fig. 6, Fig. 7 demonstrates the improved performance of AFT materials compared to QT materials. The AFT materials (σ_B = 950 MPa and 1058 MPa) showed results

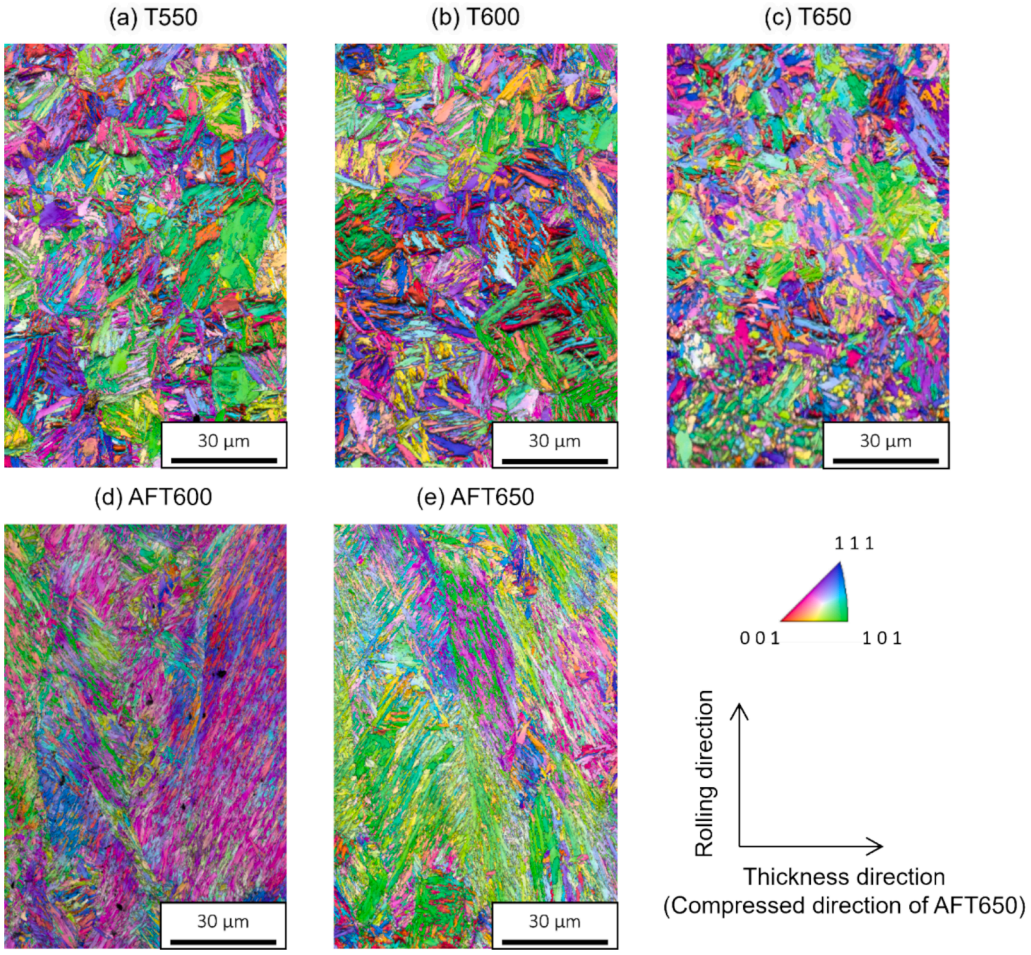

Fig. 4. Microstructures of QT and AFT materials observed via EBSD: (a) T550, (b) T600, (c) T650, (d) AFT600, (e) AFT650.

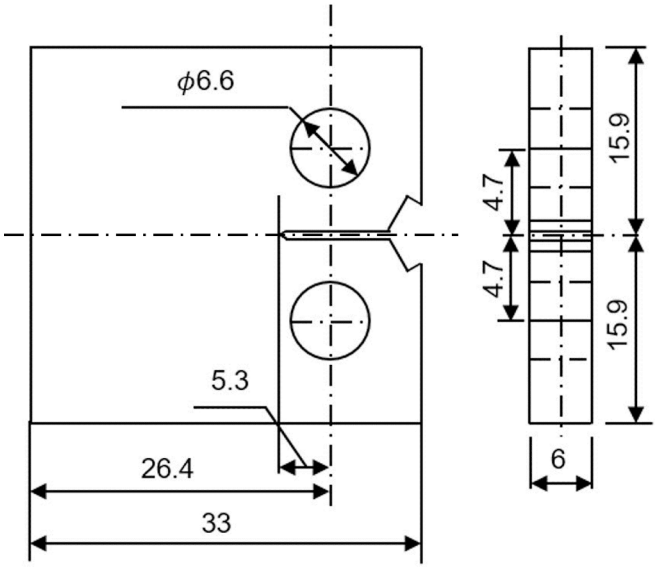

Fig. 5. Shape and dimensions of CT specimen.

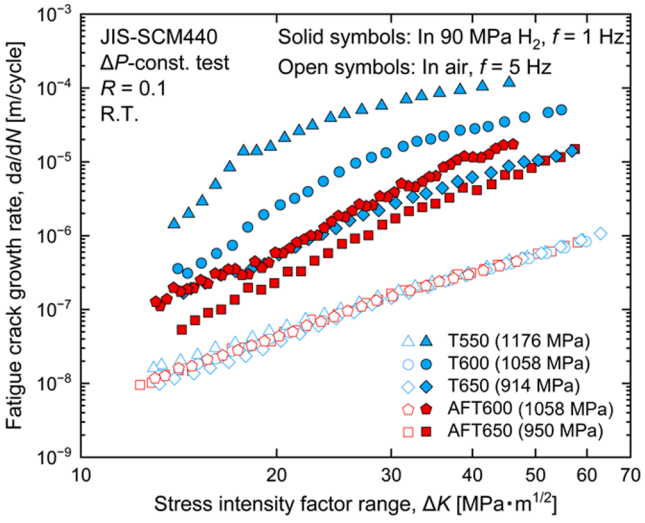

Fig. 6. FCG rate as a function of the stress intensity factor range in air and in 90 MPa hydrogen gas.

comparable to, and in some cases superior to, to T650 (σ_B = 914 MPa) the lower-strength QT material, all of which exhibited cycle-dependent behavior. The remaining QT materials (σ_B = 1058 MPa and 1176 MPa) showed clear time-dependence. Despite having the same strength level, the relative FCG rate of T600 was one order of magnitude superior to its AFT counterpart, AFT600.

3.2. Fractographic observation

Fig. 8 shows the fracture surfaces of the QT and AFT materials after ΔP-constant tests in air. Two loading levels were selected for

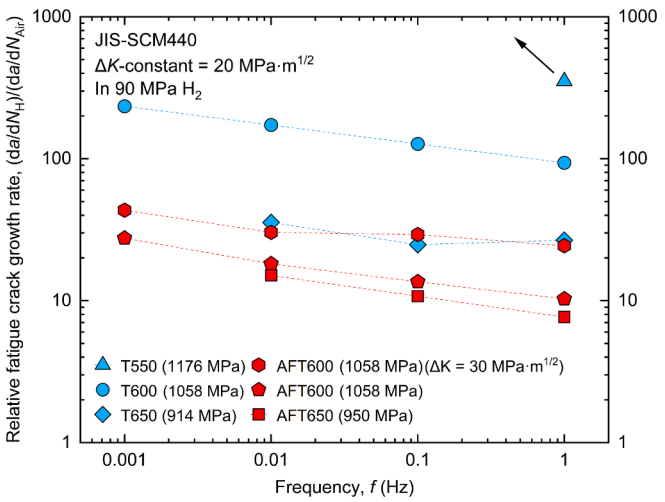

Fig. 7. Relative FCG rate as a function of loading frequency.

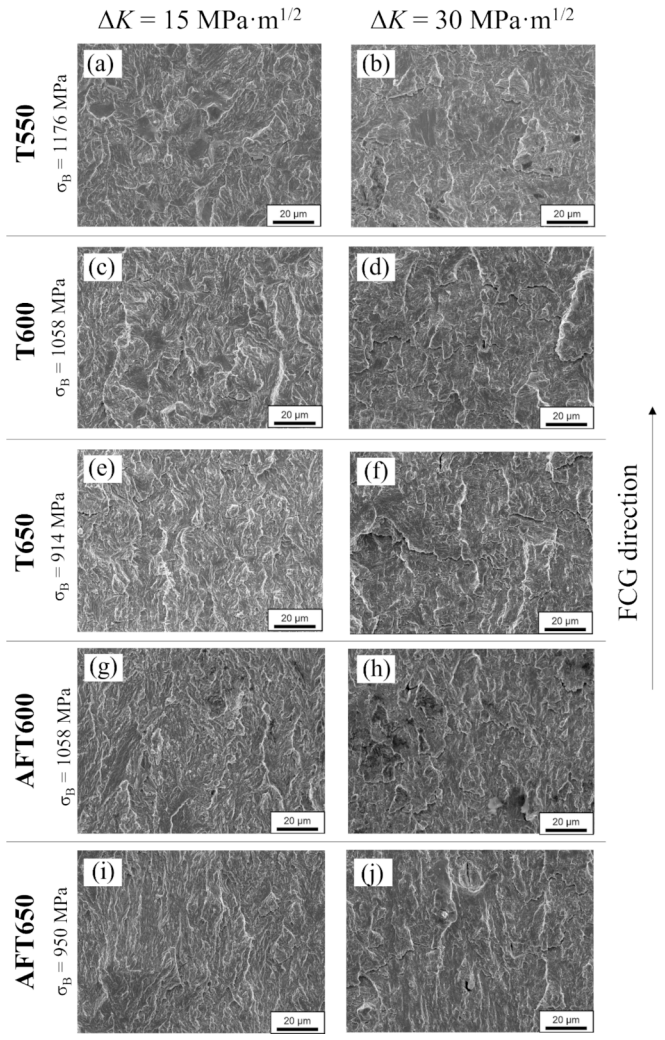

Fig. 8. Fracture surfaces of AFT and QT materials at two ΔK levels in air.

comparison: $\Delta K = 15$ and 30 MPa·m$^{1/2}$. Note that the compression direction during the ausforming was parallel to the thickness direction of the CT specimen. The fracture surfaces in air showed no significant differences at different ΔK levels, exhibiting typical ductile transgranular fracture characteristics. AFT materials also did not exhibit any notable differences compared to the QT materials.

Fig. 9 shows the fracture surfaces of the QT and AFT materials after ΔP-constant tests in 90 MPa hydrogen gas at $\Delta K = 15$ MPa·m$^{1/2}$ and 30 MPa·m$^{1/2}$. In T550 and T600, the fracture surfaces in hydrogen exhibit several types of fractures such as intergranular cracks, crevices (longitudinal cracks), indicated by white and red arrows in Fig. 9, which are distinct from those in air. In contrast, T650 did not exhibit intergranular fractures. On the other hand, in the AFT materials, no brittle fracture surfaces such as intergranular fractures were observed; instead, ductile transgranular fracture was observed. At $\Delta K = 30$ MPa·m$^{1/2}$, large crevices are observed on both QT and AFT materials (cf. red arrows in Fig. 9). They appear larger in AFT600 and AFT650 (cf. Fig. 9(h), 9(j)), but are not exclusive to AFT materials, as seen in T600 (Fig. 9(d)).

Fig. 10 shows examples of fracture paths on the mid-thickness of CT specimens of T650 and AFT650 in 90 MPa hydrogen gas at $\Delta K = 20$ MPa·m$^{1/2}$. The yellow dashed line in the figure indicates the crack path having misorientations between 21° and 47°, which is likely to be identified as PAGBs [35–37]. The figure shows that cracking along PAGBs was observed in QT materials but not in AFT materials. Between air and hydrogen gas, no increase in the frequency of intergranular cracking, secondary cracks, or branching was observed in AFT650 in hydrogen gas. This suggests that the change in microstructure due to ausforming may suppress intergranular cracking under high-pressure

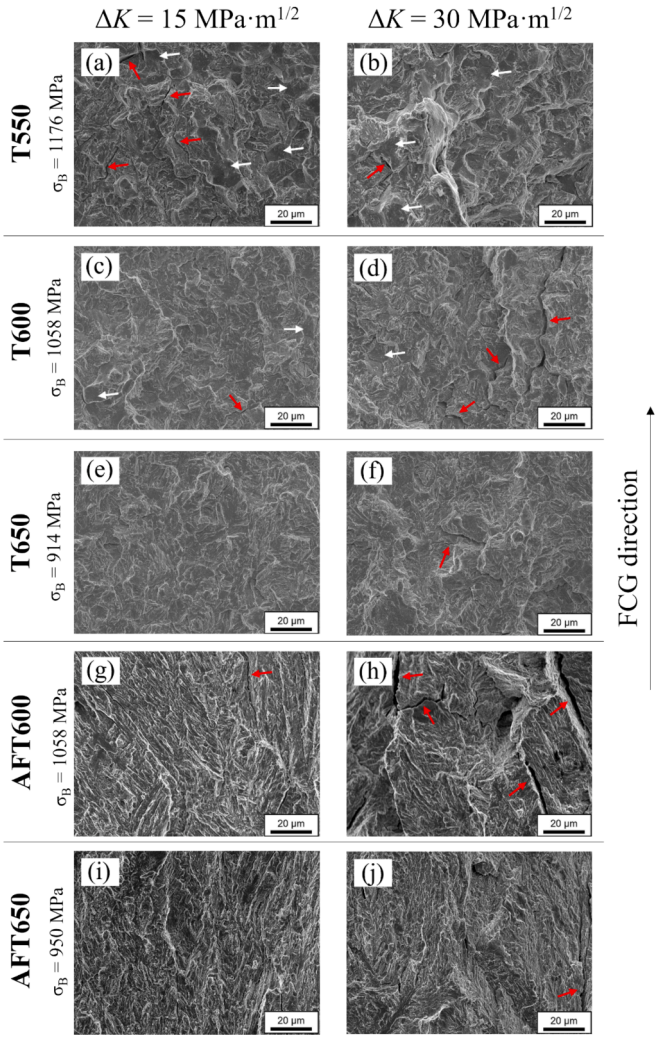

Fig. 9. Fracture surfaces of AFT and QT materials at two ΔK levels in hydrogen (white arrows indicate intergranular fractures and red arrows denote crevices). (For interpretation of the references to colour in this figure legend, the reader is referred to the web version of this article.)

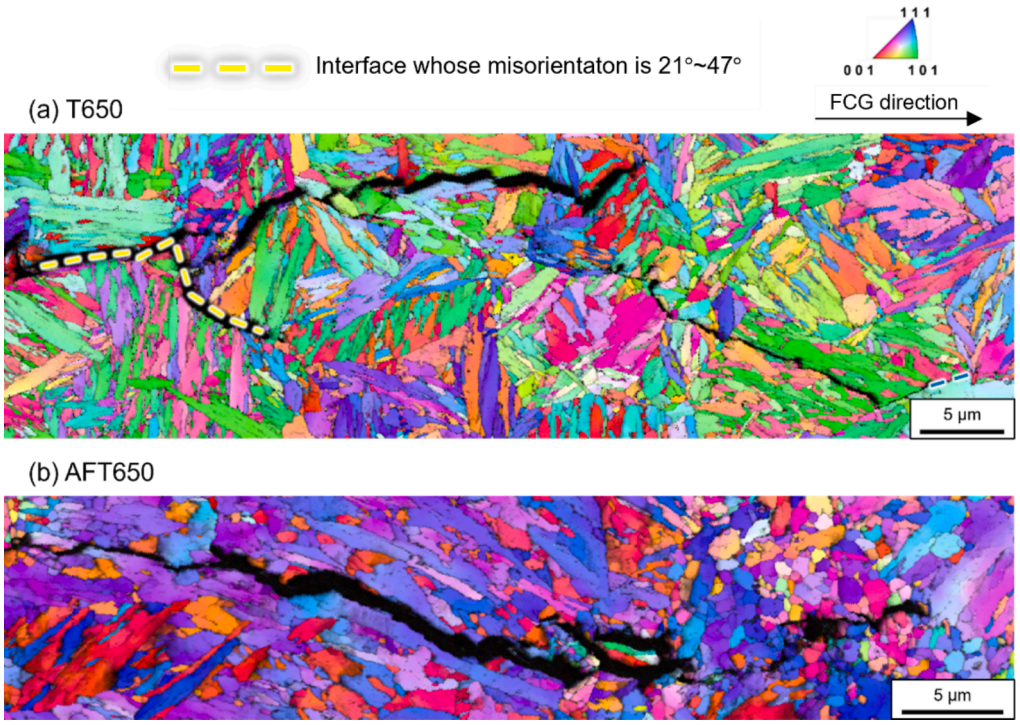

Fig. 10. Examples of mid-thickness fracture paths in 90 MPa hydrogen gas at $\Delta K = 20$ MPa·m$^{1/2}$ and $f = 1$ Hz for (a) T650 and (b) AFT650.

hydrogen gas.

4. Discussion

4.1. Exceptional hydrogen resistance of ausformed materials

Fig. 11 shows the relationship between relative FCG rate, $(da/dN)_H/(da/dN)_{Air}$, and tensile strength, σ_B, for several commercial-grade low-alloy and carbon steels in 90–115 MPa hydrogen gas [12,13]. In the range of $\sigma_B < 900$ MPa, the relative FCG rates fall within a band of 10–40 times, indicating that the materials exhibit cycle-dependent acceleration. In contrast, in the range of $\sigma_B > 900$ MPa, most of the materials display time-dependent acceleration with rates much greater than 10–40 times. It has been reported that, in this high-strength regime, loading frequency has a significant impact on FCG acceleration, as shown in the previous studies [12,13,38]. However, the FCG rates of AFT materials remain at a lower level even though their σ_B values far exceeds 900 MPa. The results indicate that, for equivalent strength, AFT materials demonstrate exceptional FCG resistance in high-pressure hydrogen gas compared to their QT counterparts.

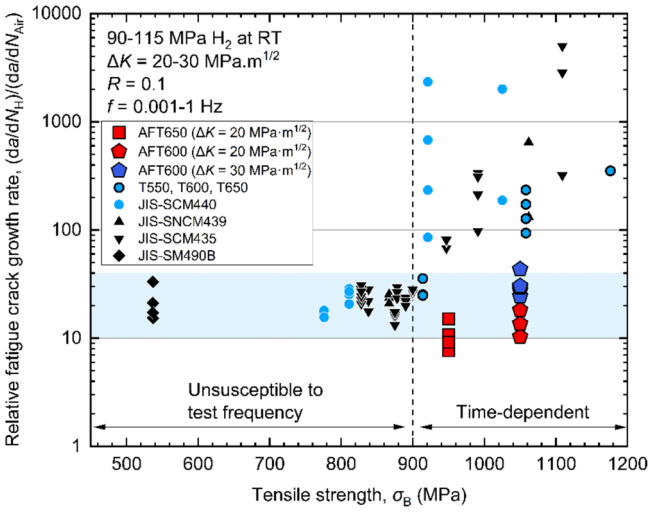

Fig. 11. Relationship between the relative FCG rate and tensile strength.

4.2. Causes of the exceptional crack-growth resistance of ausformed materials in hydrogen gas

Based on a series of previous studies, two possible dominating mechanisms for crack-growth resistance can be identified: (i) microstructural morphology, e.g., grain refinement [39–42] and grain elongation [43–45], and (ii) changes in the cohesive strength of interfaces under the influence of hydrogen [46–48]. In this subsection, we discuss how these mechanisms potentially contribute to improving the resistance to hydrogen-assisted FCG.

(i) Role of microstructural morphology

As mentioned earlier in this paper (cf. Fig. 4), the microstructure of AFT materials is finer and more flattened compared to that of QT materials. Several researchers have studied the influence of grain size on the resistance to HE [49–52]. Nie et al. [53] concluded that ultrafine elongated grain (UFEG) structures exhibit higher HE resistance, as hydrogen-induced cracking follows the UFEG structure. Generally, a crack following the grain boundary is subjected to a deflection at each grain boundary (GB) triple junction [54], where the energy required for intergranular fracture increases with an increase in the deflection angle.

Fig. 12 presents a schematic illustrating the differences in grain boundary interface shape between QT and AFT materials, which explains the varying susceptibility to intergranular cracking in these microstructures. For example, flattened grains, offer fewer opportunities for the crack tip to encounter grain boundaries. Additionally, the planar crack surface intersects with wave-shaped grain boundary interfaces, where the crack tip encounters irregular, interlocking boundaries. In the figure, the larger PAG size in the AFT materials is depicted in the schematic as a result of their higher austenitizing temperature compared to the QT materials. In AFT materials, compression during their

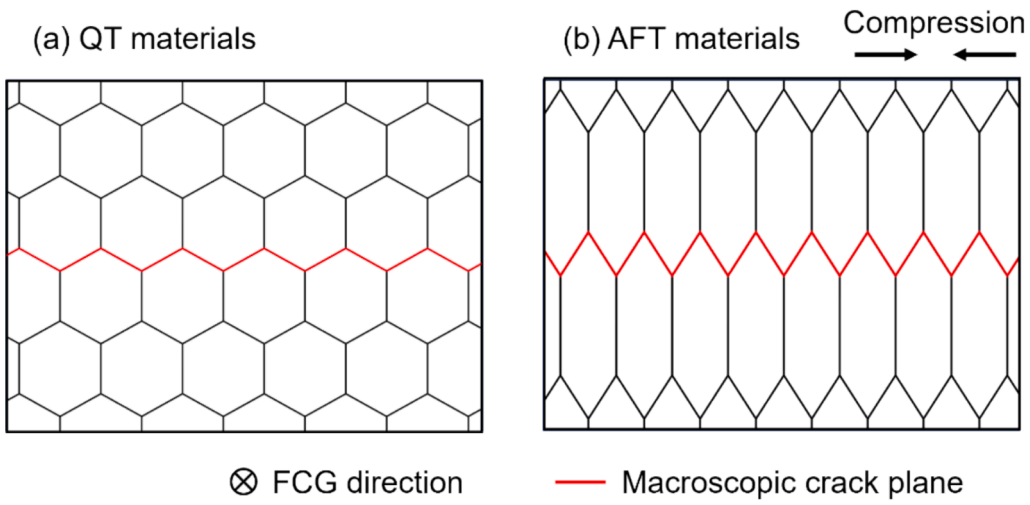

Fig. 12. Schematics showing the intersection of the planar crack surface with grain boundaries in (a) QT and (b) AFT materials.

processing leads to grains exhibiting greater flatness and elongation compared to those in QT materials. When a crack propagates along the GBs, it generates a more complex three-dimensional crack path. This path, characterized by increased microscopic crack twisting, reduces the local normal stress ahead of the crack (*i.e.*, driving force for GB separation) even under an equivalent ΔK, thereby making it more difficult for hydrogen to promote grain boundary separation. In addition to these mechanical aspects, several studies have directly linked higher twist angles in grain boundaries to increased fatigue crack resistance from a crystallographic perspective [55,56]. Zhang et al. [57] importantlty demonstrated that grain boundary slip system activation is enhanced at higher twist angles near the crack tip, leading to the formation of multiple potential fracture planes and increasing the likelihood of transgranular cracking. Consequently, AFT materials show reduced susceptibility to intergranular cracking.

Several researchers also emphasized the effect of grain size on stress concentration at grain boundaries in various steels [58–62]. For example, Bai et al. [63] observed that after interrupting a tensile test with notched specimens in a hydrogenated condition, the number and length of cracks in coarser-grained specimens were significantly greater than in ultrafine-grained specimens. They proposed that the finer-grained specimens exhibited lower stress concentration at grain boundaries, leading to reduced hydrogen accumulation during deformation. Similarly, for AFT materials, the finer, flattened grains can enhance FCG resistance by increasing deflection angles and reducing stress concentrations at grain boundaries.

Deng et al. [64] found that in medium-carbon steels, the orientation of martensite laths ahead of the crack tip dictates the direction of crack-growth in air. Similarly, Ueki et al. [65] conducted FCG tests on a low-alloy steel in air and observed that fatigue crack propagation encountered higher resistance when perpendicular to the habit plane rather than parallel. In another study, Ueki et al. [66] demonstrated that when packets were nearly perpendicular to the notch direction, crack propagation was driven by the accumulation of damage from out-of-plane slip gliding, leading to higher FCG resistance. These findings indicate that orientation may play a crucial role in FCG resistance in hydrogen environments, even though these experiments were performed in air.

As discussed above, in martensitic steels, changes in microstructure morphology, such as grain refinement and grain flattening, may influence HE resistance. However, this study revealed a significant change in the fracture morphologies: in QT materials, FCG was predominantly intergranular, whereas AFT materials exhibited little, if any, intergranular fracture (cf. Fig. 9). Thus, while the microstructure morphology of AFT materials (i.e., grain refinement and grain flattening) may indirectly influence fracture morphology, it may not be the primary factor contributing to their exceptional HE resistance.

(ii) Change in the cohesive strength of interfaces

Several studies have highlighted the significant role of grain boundary morphology in determining resistance to hydrogen-induced degradation [67–71]. Yusa et al. [26] identified stress concentration due to coarse cementite along PAGBs as a major factor weakening these boundaries and making them susceptible to delayed fracture. This approach allowed significant refinement of intergranular cementite by introducing more concave and convex PAGBs. These changes in both PAGB and cementite morphology may be key factors contributing to the enhanced FCG resistance of AFT materials in hydrogen gas. To explore these aspects, we are conducting a series of microscopic observations of GB fractures in AFT materials using SEM and EBSD. The results will be presented in a forthcoming paper, along with a more detailed discussion of the mechanisms behind the improved hydrogen resistance of AFT materials.

As indicated by red arrows in Fig. 9, numerous crevices were observed on the fracture surfaces of T600 as well as AFT650 and AFT600. These crevices can form due to tensile normal stress in the thickness direction of the specimen under plane-strain conditions near the crack tip. Their presence suggests that not all grain boundaries possess high resistance to hydrogen-induced fracture, even in AFT materials. Notably, these crevices may provide stress relaxation ahead of the crack tip [72] by reducing hydrostatic stress within the material and alleviating hydrogen accumulation at critical sites. As a result, these longitudinal cracks may help suppress the acceleration of main crack propagation.

4.3. Possible strategies for further material improvement

Considering that a growing crack front encounters multiple grains, time-dependent crack-growth along PAGBs results from the hydrogen-assisted fracture of individual grains and their subsequent coalescence. Whether a grain fractures intergranularly or transgranularly depends on the balance between the driving force (e.g., local stress) and the resistance force (e.g., fracture stress of the grain boundaries). According to elastic–plastic fracture mechanics [73], the driving force increases with the material's yield strength. The resistance force varies depending on the orientation of the boundary surface and the variability of boundary strength [12].

Fig. 13 schematically illustrates the competitive relationship between the driving and resistance forces for boundary cracking, with the higher and lower bell curves representing the strength distribution of

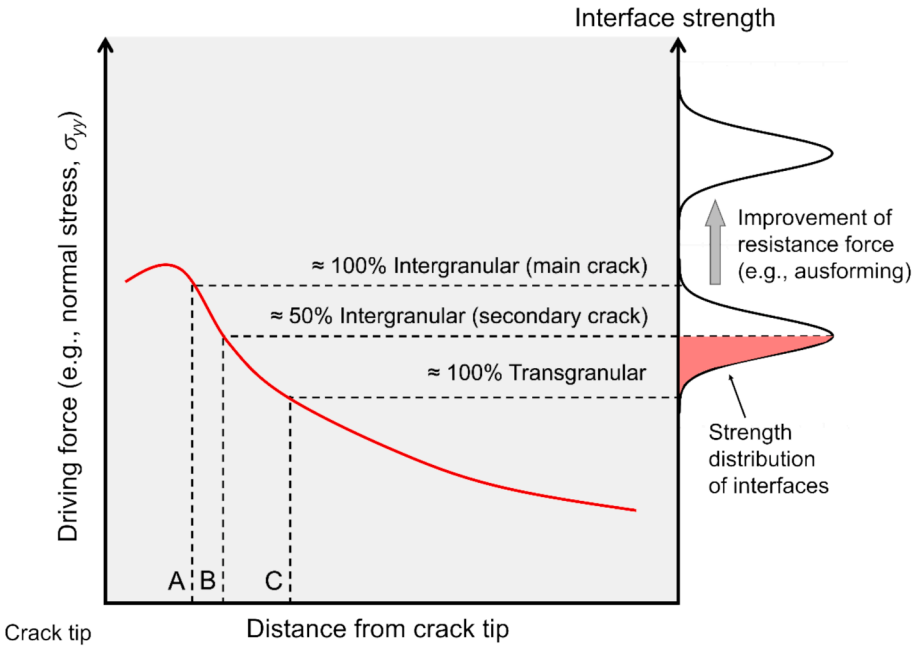

Fig. 13. Schematic of the relationship between driving forces and resistance forces.

interfaces in AFT and QT materials, respectively. The red-colored area within the lower bell curve indicates the fracture probability at a specific distance from the crack tip. The more filled the bell curve, the higher the fracture probability. This figure shows that despite similar strength levels in both materials (i.e., AFT and QT), the fracture probability is consistently higher for QT materials. It is also noted that fracture probability decreases with increasing distance from the crack tip. The driving force varies with the material's strength, while the resistance force is influenced by the material's microstructure, including factors such as PAGBs and the presence of carbides at grain boundaries.

As discussed in the previous sections, the mechanisms governing the resistance force have yet to be clarified either phenomenologically or quantitatively. Future steps in our research include assessing the FCG rate of higher-strength AFT materials to confirm the characteristics observed so far. After conducting FCG tests on AFT and QT materials with $\sigma_B = 950$ MPa and $= 1058$ MPa, our next focus will be on evaluating the performance of AFT materials with a tensile strength of around 1150 MPa. Comparing T550 ($\sigma_B \approx 1150$ MPa) with an AFT material of similar strength would provide valuable insights. Additionally, we aim to elucidate the microscopic mechanisms contributing to the exceptional fatigue resistance of AFT materials in hydrogen through detailed observations and analyses of crack paths and fracture surfaces.

5. Conclusions

In order to explore higher-strength steels with sufficient fatigue crack-growth (FCG) resistance in a hydrogen gas environment, we focused on improving the microstructure through the ausforming process. Various ausformed and tempered (AFT) specimens of low-alloy steel, JIS-SCM440, were produced and subjected to a series of FCG tests in air and 90 MPa hydrogen gas. The results were compared to non-ausformed specimens of the same material. The key conclusions are as follows:

1. AFT materials with tensile strengths ranging from 950 MPa to 1058 MPa exhibited satisfactory FCG resistance in hydrogen, even when their strengths exceeded the application limit of conventionally heat-treated materials (i.e., greater than 900 MPa).
2. Observations of fracture surfaces and crack paths revealed that the enhanced hydrogen resistance of AFT materials is attributed to the suppression of intergranular cracking.
3. Possible mechanisms for the enhanced FCG resistance of AFT materials were discussed, focusing on microstructure refinement, grain elongation, and changes in the cohesive strength of interfaces. While microstructure morphology can influence resistance to hydrogen embrittlement, the significant reduction of intergranular cracking in AFT materials suggests that other factors, such as changes in the cohesive strength of interfaces, may play more crucial role.
4. While our study offered insights into potential strategies for further improving the FCG resistance of AFT materials in high-pressure hydrogen environments, a definitive conclusion among the hypotheses remains elusive. The complexity of the interactions indicates that further testing and observation are necessary. In our forthcoming paper, we will present additional results on higher-strength AFT materials, along with observations and analyses that clarify the underlying mechanisms.

CRediT authorship contribution statement

Timothee Redarce: Writing – review & editing, Writing – original draft, Methodology, Investigation, Formal analysis, Data curation, Conceptualization. **Keiichiro Iwata:** Data curation. **Yuhei Ogawa:** Writing - review & editing, Supervision, Conceptualization. **Kaneaki Tsuzaki:** Writing – review & editing, Material fabrication. **Akinobu Shibata:** Writing – review & editing, Material fabrication. **Hisao Matsunaga:** Writing – review & editing, Validation, Supervision, Conceptualization.

Declaration of competing interest

The authors declare that they have no known competing financial interests or personal relationships that could have appeared to influence the work reported in this paper.

Acknowledgements

This work was supported by the MEXT Program: Data Creation and Utilization Type Material Research and Development Project (Grant

Number: JPMXP1122684766) and the establishment of University Fellowships towards the Creation of Science and Technology Innovation (Grant Number: JPMJFS2132). The authors gratefully acknowledge Mr. Masaki Kobayashi and Mr. Kazuhiko Iida of the Materials Melting and Manufacturing Unit at NIMS for their dedicated cooperation in material fabrication.

Data availability

Data will be made available on request.

References

[1] S. Agbo, F. Davaripour, and K. Roy, "Effects of Hydrogen Embrittlement on the Fracture Toughness of High-Strength Steel Structures," Oct. 2022. doi: 10.1115/IPC2022-87174.
[2] Yaguchi H. Examples of fractured steel parts during actual usage due to hydrogen embrittlement and consideration regarding the behavior of hydrogen at the prior austenite grain boundary. ISIJ Int 2023. https://doi.org/10.2355/isijinternational.ISIJINT-2023-264.
[3] Murakami Y, Yamabe J, Matsunaga H. Microscopic mechanism of hydrogen embrittlement in fatigue and fracture. Key Eng Mater Trans Tech Publications Ltd 2014:3–13. https://doi.org/10.4028/www.scientific.net/KEM.592-593.3.
[4] Gangloff RP, Somerday BP. Gaseous hydrogen embrittlement of materials in energy technologies: the problem, its characterisation and effects on particular alloy classes. Elsevier; 2012.
[5] Jemblie L, et al. Safe pipelines for hydrogen transport. Int J Hydrogen Energy 2024. https://doi.org/10.1016/j.ijhydene.2024.06.309.
[6] Myhre A, et al. Assessing fracture toughness of vintage and modern X65 pipeline steels under in situ electrochemical hydrogen charging using advanced testing methodology. Eng Fract Mech 2024;301:110026. https://doi.org/10.1016/j.engfracmech.2024.110026.
[7] Kim JH, et al. Influence of austenite grain boundary misorientation on hydrogen-induced intergranular crack propagation in a medium carbon martensitic steel. Acta Mater 2024;274:120036. https://doi.org/10.1016/j.actamat.2024.120036.
[8] Shibata A, et al. Local crack arrestability and deformation microstructure evolution of hydrogen-related fracture in martensitic steel. Corros Sci 2024;233:112092. https://doi.org/10.1016/j.corsci.2024.112092.
[9] Trautmann A, Mori G, Oberndorfer M, Bauer S, Holzer C, Dittmann C. Hydrogen uptake and embrittlement of carbon steels in various environments. Materials 2020;13(16). https://doi.org/10.3390/MA13163604.
[10] Matsunaga H, Yamabe J, Takakuwa O, Ogawa Y, Matsuoka S. In: Hydrogen Gas Embrittlement: Mechanisms, Mechanics, and Design. Elsevier; 2024. https://doi.org/10.1016/C2020-0-01846-3.
[11] Matsuoka S, Yamabe J, Matsunaga H. Criteria for determining hydrogen compatibility and the mechanisms for hydrogen-assisted, surface crack growth in austenitic stainless steels. Eng Fract Mech 2016;153:103–27. https://doi.org/10.1016/j.engfracmech.2015.12.023.
[12] Setoyama A, et al. Transition mechanism of cycle- to time-dependent acceleration of fatigue crack-growth in 0.4 %C Cr-Mo steel in a pressurized gaseous hydrogen environment. Int J Fatigue Oct. 2022;163. https://doi.org/10.1016/j.ijfatigue.2022.107039.
[13] Matsuoka S, Matsunaga H, Yamabe J, Hamada S, Iijima T. Various strength properties of SCM435 and SNCM439 low-alloy steels in 115 MPa hydrogen gas and proposal of design guideline. Trans JSME (Japanese) 2017;83(854):17-00264. https://doi.org/10.1299/transjsme.17-00264.
[14] Nibur KA, Somerday BP, Marchi CS, Foulk III JW, Dadfarnia M, Sofronis P. The relationship between crack-tip strain and subcritical cracking thresholds for steels in high-pressure hydrogen gas. Metall Mater Trans A Phys Metall Mater Sci 2013;44(1):248–69. https://doi.org/10.1007/s11661-012-1400-5.
[15] Ogawa Y, Umakoshi K, Nakamura M, Takakuwa O, Matsunaga H. Hydrogen-assisted, intergranular, fatigue crack-growth in ferritic iron: Influences of hydrogen-gas pressure and temperature variation. Int J Fatigue 2020;140:105806. https://doi.org/10.1016/j.ijfatigue.2020.105806.
[16] Matsuoka S, Takakuwa O, Okazaki S, Yoshikawa M, Yamabe J, Matsunaga H. Peculiar temperature dependence of hydrogen-enhanced fatigue crack growth of low-carbon steel in gaseous hydrogen. Scr Mater 2018;154. https://doi.org/10.1016/j.scriptamat.2018.05.035.
[17] Wada K, Yamabe J, Ogawa Y, Takakuwa O, Iijima T, Matsunaga H. Comparative study of hydrogen-induced intergranular fracture behavior in Ni and Cu–Ni alloy at ambient and cryogenic temperatures. Mater Sci Eng A 2019;766:138349. https://doi.org/10.1016/j.msea.2019.138349.
[18] Komoda R, et al. Mitigation of hydrogen embrittlement of iron and steels by carbon monoxide in gaseous H2. Int J Hydrogen Energy 2024. https://doi.org/10.1016/j.ijhydene.2024.04.071.
[19] Okumura K, Motoyama K, Matsunaga H. Fatigue crack-growth properties of ductile cast iron in hydrogen gas with oxygen impurity at various temperatures. Eng Fail Anal 2024;158:108012. https://doi.org/10.1016/j.engfailanal.2024.108012.
[20] Somerday BP, Sofronis P, Nibur KA, San Marchi C, Kirchheim R. Elucidating the variables affecting accelerated fatigue crack growth of steels in hydrogen gas with low oxygen concentrations. Acta Mater 2013;61(16):6153–70. https://doi.org/10.1016/j.actamat.2013.07.001.
[21] Pinson M, Springer H, Depover T, Verbeken K. The role of cementite on the hydrogen embrittlement mechanism in martensitic medium-carbon steels. Mater Sci Eng A 2022;859:144204. https://doi.org/10.1016/j.msea.2022.144204.
[22] JPEC-TD 0003, "Jpec-td, 0003, Technical document for safety use of pressure storage vessels made of low alloy steels used in hydrogen refueling stations, Japan Petroleum Energy Center (2020)," 2020.
[23] Sugimoto K, Itoh M, Hojo T, Hashimoto S, Ikeda S, Arai G. Microstructure and Mechanical Properties of Ausformed Ultra High-Strength TRIP-Aided Steels. Mater Sci Forum 2007;539–543:4309–14. https://doi.org/10.4028/www.scientific.net/MSF.539-543.4309.
[24] V. F. Zackay and W. W. Gerberich, "The Potentiality Of Ausform Steels For Prestressing".
[25] Kimura Y, Moronaga T, Inoue T. Influence of thermomechanical treatment on delayed fracture property of Mo-bearing medium-carbon steel. ISIJ Int 2022;62(2):377–88. https://doi.org/10.2355/isijinternational.ISIJINT-2021-407.
[26] Yusa S, Hara T, Tsuzaki K. Grain boundary carbide structure in tempered martensitic steel with serrated prior austenite grain boundaries. Nippon Kinzoku Gakkaishi/J Japan Inst Metals 2000;64:1230–8. https://doi.org/10.2320/jinstmet1952.64.12_1230.
[27] Maki T, Furuhara T, Tsuji N, Morito S, Miyamoto G, Shibata A. Thermomechanical processing of steel –past, present and future–. Tetsu-to-Hagane 2014;100:1062–75. https://doi.org/10.2355/tetsutohagane.100.1062.
[28] ASTM E647-15, "Test method for measurement of fatigue crack growth rates," ASTM International, 2013, doi: 10.1520/E0647-15E01.
[29] Y. Manabe, "Hot Isostatic Pressing and High Hydrogen Pressure Testing Equipment," 2009. doi: doi: 10.4131/jshpreview.19.281.
[30] J. M. Barsom E J Imhof and S. T. Rolfe, "Fatigue-crack propagation in high yield-strength steels".
[31] Takeo Y, Kiyoshi S. The effect of frequency on fatigue crack propagation rate and striation spacing in 2024-T3 aluminium alloy and SM-50 steel. Eng Fract Mech 1976;8(1):81–8. https://doi.org/10.1016/0013-7944(76)90078-3.
[32] Nishikawa H, Oda Y, Noguchi H. Loading-frequency effects on fatigue crack growth behavior of a low carbon steel JIS S10C in hydrogen gas environment. J Solid Mech Mater Eng 2011;5(2):104–16. https://doi.org/10.1299/jmmp.5.104.
[33] P. Paris, A. Director, and F. Erdogan, "A Critical Analysis of Crack Propagation Laws," 1963. [Online]. Available: http://asmedigitalcollection.asme.org/fluidsengineering/article-pdf/85/4/528/5763569/528_1.pdf.
[34] Chen T, Koyama M, Ogawa Y, Matsunaga H, Akiyama E. Martensite boundary characteristics on cycle- and time-dependent fatigue crack growth paths of tempered lath martensitic steels in a 90 mpa gaseous hydrogen atmosphere. Metall Mater Trans A 2023;54. https://doi.org/10.1007/s11661-023-07041-9.
[35] Karthikeyan T, Vijayalakshmi M. Orientational equidistance method for solving orientation relationship from product variants: application to steel. Trans Indian Inst Met 2018;71(2):421–36. https://doi.org/10.1007/s12666-017-1172-0.
[36] Thangaraj K, Dash M, Saibaba S, Vijayalakshmi M. Estimation of martensite feature size in a low-carbon alloy steel by microtexture analysis of boundaries. Micron 2015;68. https://doi.org/10.1016/j.micron.2014.09.008.
[37] F. Archie and S. Zaefferer, Prior austenite grain boundaries in lath martensite: correlation between the crystallographic character and the fracture susceptibility. 2018.
[38] Yoshikawa M, Matsuo T, Tsutsumi N, Matsunaga H, Matsuoka S. Effects of hydrogen gas pressure and test frequency on fatigue crack growth properties of low carbon steel in 0.1-90 MPa hydrogen gas. Trans JSME (in Japanese) 2014;80(817):SMM0254. https://doi.org/10.1299/transjsme.2014smm0254.
[39] Matsushita A, Ueki S, Mine Y, Takashima K. Comparative study of microstructure-sensitive fatigue crack propagation in coarse- and fine-grained microstructures between stable and metastable austenitic stainless steels using miniature specimen. ISIJ Int 2021;61(5):1688–97. https://doi.org/10.2355/isijinternational.ISIJINT-2020-659.
[40] Chang Y, Pan X, Zheng L, Hong Y. Microstructure refinement and grain size distribution in crack initiation region of very-high-cycle fatigue regime for high-strength alloys. Int J Fatigue 2020;134:105473. https://doi.org/10.1016/j.ijfatigue.2020.105473.
[41] Leitner T, Hohenwarter A, Ochensberger W, Pippan R. Fatigue crack growth anisotropy in ultrafine-grained iron. Acta Mater 2017;126:154–65. https://doi.org/10.1016/j.actamat.2016.12.059.
[42] Hohenwarter A, Pippan R. Anisotropic fracture behavior of ultrafine-grained iron. Mater Sci Eng A 2010;527(10):2649–56. https://doi.org/10.1016/j.msea.2009.12.033.
[43] Hohenwarter A, Pippan R. Fracture toughness evaluation of ultrafine-grained nickel. Scr Mater 2011;64(10):982–5. https://doi.org/10.1016/j.scriptamat.2011.02.007.
[44] Hohenwarter A, Pippan R. Fracture and fracture toughness of nanopolycrystalline metals produced by severe plastic deformation. Philos Trans A Math Phys Eng Sci 2015;373. https://doi.org/10.1098/rsta.2014.0366.
[45] Leitner T, Hohenwarter A, Pippan R. Revisiting fatigue crack growth in various grain size regimes of Ni. Mater Sci Eng A 2015;646:294–305. https://doi.org/10.1016/j.msea.2015.08.071.
[46] Fernández-Sousa R, Betegón C, Martínez-Pañeda E. Cohesive zone modelling of hydrogen assisted fatigue crack growth: The role of trapping. Int J Fatigue 2022;162:106935. https://doi.org/10.1016/j.ijfatigue.2022.106935.
[47] Harris ZD, Lawrence SK, Medlin DL, Guetard G, Burns JT, Somerday BP. Elucidating the contribution of mobile hydrogen-deformation interactions to hydrogen-induced intergranular cracking in polycrystalline nickel. Acta Mater 2018;158:180–92. https://doi.org/10.1016/j.actamat.2018.07.043.

[48] Shishvan SS, Csányi G, Deshpande VS. Hydrogen induced fast-fracture. J Mech Phys Solids 2020;134:103740. https://doi.org/10.1016/j.jmps.2019.103740.
[49] S. Matsuyama, "Effects of Tempering, Prior-austenite Grain Size and Shape of Test Specimen on the Delayed Fracture of Low-alloyed Steels," 鉄と鋼, vol. 58, no. 3, pp. 395–410, 1972, doi: 10.2355/tetsutohagane1955.58.3_395.
[50] Lessar JF, Gerberich WW. Grain size effects in hydrogen-assisted cracking. Metall Trans A 1976;7(7):953–60. https://doi.org/10.1007/BF02644060.
[51] Padmanabhan R, Wood WE. Hydrogen induced cracking in a low alloy steel. Metall Trans A 1983;14(11):2347–56. https://doi.org/10.1007/BF02663310.
[52] Hui W, et al. Delayed fracture behavior of ultrafine grained high strength steel. Acta Metallurgica Sinica -Chinese Edition- Jun. 2004;40:561–8.
[53] Nie Y, Kimura Y, Inoue T, Yin F, Akiyama E, Tsuzaki K. Hydrogen embrittlement of a 1500-MPa tensile strength level steel with an ultrafine elongated grain structure. Metall Mater Trans A 2012;43(5):1670–87. https://doi.org/10.1007/s11661-011-0974-7.
[54] Ohtani H, McMahon CJ. Modes of fracture in temper embrittled steels. Acta Metall 1975;23(3):377–86. https://doi.org/10.1016/0001-6160(75)90131-5.
[55] Nakanishi D, Kawabata T, Aihara S. Brittle crack propagation resistance inside grain and at high angle grain boundary in 3% Si-Fe alloy. Acta Mater 2018;144:768–76. https://doi.org/10.1016/j.actamat.2017.11.020.
[56] Jain V, Chatterjee A, Patra S, Chakrabarti D, Ghosh A. Effect of tilt and twist angles on the cleavage crack propagation in ferritic steel. Int J Fract 2020;225(1):115–21. https://doi.org/10.1007/s10704-020-00467-x.
[57] Zhang X, Dunne FPE. 3D CP-XFEM modelling of short crack propagation interacting with twist/tilt nickel grain boundaries. J Mech Phys Solids 2022;168:105028. https://doi.org/10.1016/j.jmps.2022.105028.
[58] Zan N, Ding H, Guo X, Tang Z, Bleck W. Effects of grain size on hydrogen embrittlement in a Fe-22Mn-0.6C TWIP steel. Int J Hydrogen Energy 2015;40(33):10687–96. https://doi.org/10.1016/j.ijhydene.2015.06.112.
[59] Koyama M, Ichii K, Tsuzaki K. Grain refinement effect on hydrogen embrittlement resistance of an equiatomic CoCrFeMnNi high-entropy alloy. Int J Hydrogen Energy 2019;44(31):17163–7. https://doi.org/10.1016/j.ijhydene.2019.04.280.
[60] Ogawa Y, Kuriyama K, Koyama M. Dual grain size-effects on hydrogen-assisted fatigue crack growth in 1 GPa-class medium-carbon martensitic steel. Int J Hydrogen Energy 2024;50:108–15. https://doi.org/10.1016/j.ijhydene.2023.08.317.
[61] Liu G, et al. Nanostructured high-strength molybdenum alloys with unprecedented tensile ductility. Nat Mater 2013;12(4):344–50. https://doi.org/10.1038/nmat3544.
[62] Kim D-H, Moallemi M, Kim K-S, Cho H-J, Kim S-J. Correlation between grain size variation and hydrogen embrittlement in a cost-effective Fe40Mn40Ni10Cr10 austenitic medium entropy alloy. Int J Hydrogen Energy 2023;48(14):5708–17.
[63] Bai Y, Tian Y, Gao S, Shibata A, Tsuji N. Hydrogen embrittlement behaviors of ultrafine-grained 22Mn–0.6C austenitic twinning induced plasticity steel. J Mater Res 2017;32(24):4592–604. https://doi.org/10.1557/jmr.2017.351.
[64] Deng X, Lu F, Cui H, Tang X, Li Z. Microstructure correlation and fatigue crack growth behavior in dissimilar 9Cr/CrMoV welded joint. Mater Sci Eng A 2016;651:1018–30. https://doi.org/10.1016/j.msea.2015.11.081.
[65] Ueki S, Mine Y, Lu X, Chiu YL, Bowen P, Takashima K. Effect of geometric lath orientation on fatigue crack propagation via out-of-plane dislocation glide in martensitic steel. Scr Mater 2021;203:114045. https://doi.org/10.1016/j.scriptamat.2021.114045.
[66] Ueki S, Mine Y, Takashima K. Microstructure-sensitive fatigue crack growth in lath martensite of low carbon steel. Mater Sci Eng A 2020;773:138830. https://doi.org/10.1016/j.msea.2019.138830.
[67] Troiano AR. The role of hydrogen and other interstitials in the mechanical behavior of metals. Metall Microstruct Anal 2016;5(6):557–69. https://doi.org/10.1007/s13632-016-0319-4.
[68] Oriani RA, Josephic PH. Testing of the decohesion theory of hydrogen-induced crack propagation. Scr Metall 1972;6(8):681–8. https://doi.org/10.1016/0036-9748(72)90126-3.
[69] Oriani RA, Josephic PH. Equilibrium aspects of hydrogen-induced cracking of steels. Acta Metall 1974;22(9):1065–74. https://doi.org/10.1016/0001-6160(74)90061-3.
[70] Bandyopadhyay N, Kameda J, Mcmahon CJ. Hydrogen-induced cracking in 4340-type steel: effects of composition, yield strength, and H2 pressure. Metall Trans A 1983;14(4):881–8. https://doi.org/10.1007/BF02644292.
[71] Kameda J, Mcmahon C-J. Solute segregation and hydrogen-induced intergranular fracture in an alloy steel. Metall Trans A 1983;14(4):903–11. https://doi.org/10.1007/BF02644295.
[72] Rizov V. Longitudinal fracture analysis of continuously inhomogeneous beam in torsion with stress relaxation. Procedia Struct Integrity 2020;28:1212–25. https://doi.org/10.1016/j.prostr.2020.11.103.
[73] Anderson TL. In: Fracture Mechanics. CRC Press; 2017. https://doi.org/10.1201/9781315370293.